Article

Unbiased mapping of cereblon neosubstrate landscape by high-throughput proteomics

Martin Steger[1,8], Gisele Nishiguchi [2,8], Qiong Wu [3,8], Bjoern Schwalb[1,8], Bachuki Shashikadze[1], Kevin McGowan[2], Marisa Actis[2], Anup Aggarwal[2], Zhe Shi [2], Jeanine Price[2], Anand Mayasundari[2], Lei Yang [2], Anastasia H. Bednarz[1], Sophie Machata[1], Tobias Graef[1], Denis Bartoschek[1], Vadim Demichev[4], Uli Ohmayer [1], Jun Yang [3,5,6] ✉, Henrik Daub [1] ✉ & Zoran Rankovic [2,7] ✉

Molecular glue degraders (MGDs) are small molecules that co-opt the ubiquitin-proteasome system to induce degradation of target proteins, including those considered undruggable. Their discovery remains challenging due to the lack of rational design strategies and limited throughput of unbiased proteome-wide screening approaches. To address this gap, we develop a high-throughput proteomics platform based on label-free, data-independent acquisition mass spectrometry (DIA-MS), enabling integrated proteomics and ubiquitinomics profiling. Screening a diverse set of 100 cereblon (CRBN)-recruiting ligands on this platform leads to identification of a broad array of novel degraders and neosubstrates. Subsequent hit validation and structure-degradation relationship analyses guided by global proteomics reveal highly selective and potent phenyl glutarimide-based degraders targeting previously uncharacterized neosubstrates such as KDM4B, G3BP2 and VCL; none of which contain the classical CRBN β-hairpin degron. These findings underscore the power of unbiased high-throughput proteomics in MGD drug discovery and reveal a substantially expanded CRBN neosubstrate landscape beyond that defined by classical immunomodulatory imid drugs (IMiDs).

Targeted protein degradation (TPD) is a rapidly emerging drug discovery paradigm that relies on engagement of normal cellular proteolytic processes to degrade disease-associated proteins[1]. The two currently most advanced TPD approaches employ proteolysis targeting chimeras (PROTACs)[2] or molecular glue degraders (MGDs)[3]. MGDs are small molecules that can bind and alter the specificity of an E3 ligase, resulting in the recruitment, ubiquitination, and subsequent degradation of new, non-physiological substrates, commonly referred to as neosubstrates. The immunomodulatory imid drugs (IMiDs) thalidomide, lenalidomide, and pomalidomide, clinically used as the first-line therapy for multiple myeloma, were the first drugs found to exert their therapeutic effect through such a mechanism[4]. IMiDs bind to cereblon (CRBN), a substrate recognition subunit of CRL4^CRBN ligase[5], and induce degradation of the transcription factors IKZF1 and IKZF3 that are required for multiple myeloma cell survival[6,7]. Importantly, the neosubstrate recruitment is governed by MGD binding to the E3 ligase,

creating a new, neomorphic recognition surface, and does not require a ligandable pocket[8,9]. This mechanism provides an unprecedented and exciting opportunity to tackle currently undruggable therapeutic targets.

Interestingly, despite their high structural similarity, lenalidomide and pomalidomide display different protein degradation profiles. While both degrade the transcription factors IKZF1/3, only lenalidomide induces degradation of CSNK1A1 (CK1α), indicating how a small difference in degrader molecular structure can significantly alter the neosubstrate specificity. Indeed, an ever-increasing number of neosubstrates have been discovered in recent years, with each IMiD displaying distinct degradation patterns, supporting the notion that E3 ligase substrate specificity can be modulated by structural alterations of the ligand. However, prospectively designing such molecules and rationalizing the structure-degradation relationship remains highly challenging.

We recently reported the synthesis of a chemically diverse library of over 5000 CRBN ligands, which we screened against a large panel of cancer cell lines in viability assays, aiming at discovering novel degraders and cancer vulnerabilities. This proved to be a productive effort that delivered potent and selective degraders of proteins such as G1-to-S-phase transition (GSPT1)[10,11] and casein kinase 1A (CK1α)[12,13] that exhibited antiproliferative activity against a broad range of human cancer cell lines. However, despite these encouraging results, our phenotypic screening approach relied solely on cell viability as the assay readout. As a result, weak degraders or proteins that are not essential for the survival of cancer cells in our screening panel would be missed by this approach. To investigate the extent of such omissions and explore a potentially wider CRBN neosubstrate landscape, we sought to explore a more direct and proteome-wide screening approach.

Mass spectrometry (MS)-based proteomics has undergone major advancements in recent years, driven by deep learning-enhanced software and next-generation MS hardware[14–16]. These developments enable near-complete and highly reproducible proteome quantifications in high-throughput mode. A key advantage of MS-based proteomics is its unbiased, target- and E3-ligase agnostic screening capability, allowing for the simultaneous discovery of novel targets and evaluation of degrader selectivity. Despite its routine application in profiling selected degrader candidates, integrated, high-throughput screening workflows for MGD discovery remain underdeveloped.

In this work, we develop a systematic and scalable high-throughput proteomics framework for MGD discovery. To demonstrate the utility of this platform, we perform screening of a diverse set of CRBN ligands, resulting in the discovery of several exquisitely potent, selective, and structurally distinct phenyl glutarimide-based degraders of previously unreported neosubstrates.

Results

Deep proteomic screening of a molecular glue degrader library

Our IMiD-based molecular glue library was designed and synthesized based on the previously described principles and protocols[13]. To expand the chemical diversity of our library beyond IMiDs, we incorporated novel CRBN-binding cores, including the recently reported phenyl-glutarimide (PG) and other proprietary scaffolds[17]. For each chemical core, we generated a diverse set of chemical scaffolds by scanning vectors with different functionalities, applying an array of chemistries, and using a diverse set of building blocks to construct over 5000 compounds covering a broad range of chemical space and physicochemical properties. As an initial proof of concept to our screening workflow, we selected centroids from each core scaffold, which produced a set of 100 compounds representing the molecular structure coverage of the library (Supplementary Fig. 1a). We excluded scaffolds known to degrade GSPT1 or CK1α based on our phenotypic

screening campaign but included our previously reported CK1α (SJ10040) and GSPT1 (SJ6986) degraders as controls.

We next designed a multilayered proteomics screening workflow aiming to expand the number of targetable proteins through CRBN-based degraders and gain deeper insight into their mechanisms of action. To maximize the detectable proteome, we selected two cancer cell lines, Huh-7 and NB-4, displaying complementary protein expression profiles and high sensitivity to CRBN-based MGDs (Supplementary Fig. 1b). Our primary screening workflow consisted of 24-h incubation in 96-well plates of the two cell lines with compound at 10 μM concentration, followed by semi-automated proteomics sample preparation and label-free, data-independent acquisition mass spectrometry (diaPASEF)[18]. We profiled the set of one hundred compounds in triplicate across both cell lines, alongside 120 DMSO controls, resulting in 720 LC-MS runs. Following MS data processing and statistical analysis, compounds that induced >25% reduction in protein abundance were designated as primary screening hits and subsequently re-tested at a 6-h time point using global proteomics. For hits that showed significant protein downregulation at both time points, we confirmed cullin-RING E3 ligase (CRL)-dependency by co-treating cells with the respective MGD and the NEDD8-activating enzyme inhibitor MLN4924[19]. To further validate putative neosubstrates, we performed global ubiquitinomics. Proteins that exhibited rapid ubiquitination following MGD treatment were classified as bona fide CRBN neosubstrates (Fig. 1a and Supplementary Data 1).

Our proteomic screening campaign quantified an average of 10,200 protein groups in Huh-7 and 9500 in NB-4 cells, with over 98% of these retained for statistical testing after filtering for missing values. The median coefficient of variation (CV) for protein groups ($n = 3$) was about 6% in both cell lines (Supplementary Fig. 2a, b). This highlights that our single-shot MS-based screening platform detected a large proportion of the proteome expressed by a human cell line, with very high data completeness and excellent quantification precision[15,20].

We first classified the compounds based on the number of significantly induced protein downregulations. About 25% of them did not modulate proteins in either cell line, while approximately 50% induced specific changes, with 10 or fewer proteins displaying a significant reduction in abundance. The remaining compounds were more promiscuous, inducing numerous protein regulations, some of which may reflect secondary effects resulting from prolonged drug exposure (Supplementary Fig. 2c). Our control degraders, SJ6986 (GSPT1) and SJ41478 (promiscuous degrader), were excluded from the neosubstrate analyses.

We identified 35 out of 49 previously reported neosubstrates from the literature[21–24]. Of these, 33 were retained after filtering for data completeness, and 25 were significantly downregulated after 24 h of treatment with at least one compound (Supplementary Data 2). Among these, RAB28, FIZ1, ZBTB16, and ZFP91 emerged as the most frequently downregulated targets across both cell lines. In contrast, Ikaros family zinc finger proteins IKZF1, IKZF2, and IKZF3 were exclusively detected and downregulated in NB-4 cells, consistent with their immune cell-specific expression (Fig. 1b)[7]. Strong IKZF1 degraders accordingly induced broader proteome changes in NB-4 cells, suggesting secondary effects due to inhibition of IKZF1-mediated transcriptional programs (Supplementary Fig. 2d).

Seventeen of the 25 previously reported neosubstrates showed significant downregulation at the 6-h time point, and co-treatment with MLN4924 rescued their levels, consistent with a CRL-dependent mechanism (Fig. 1c). In addition to confirming previously reported CRBN neosubstrates, our screening uncovered highly selective probes for several of them, including LIMD1, GZF1, and FIZ1 (Fig. 1d and Supplementary Fig. 3)[21,23,25].

Given that intracellular ubiquitination at endogenous levels has not been demonstrated for the majority of previously reported CRBN
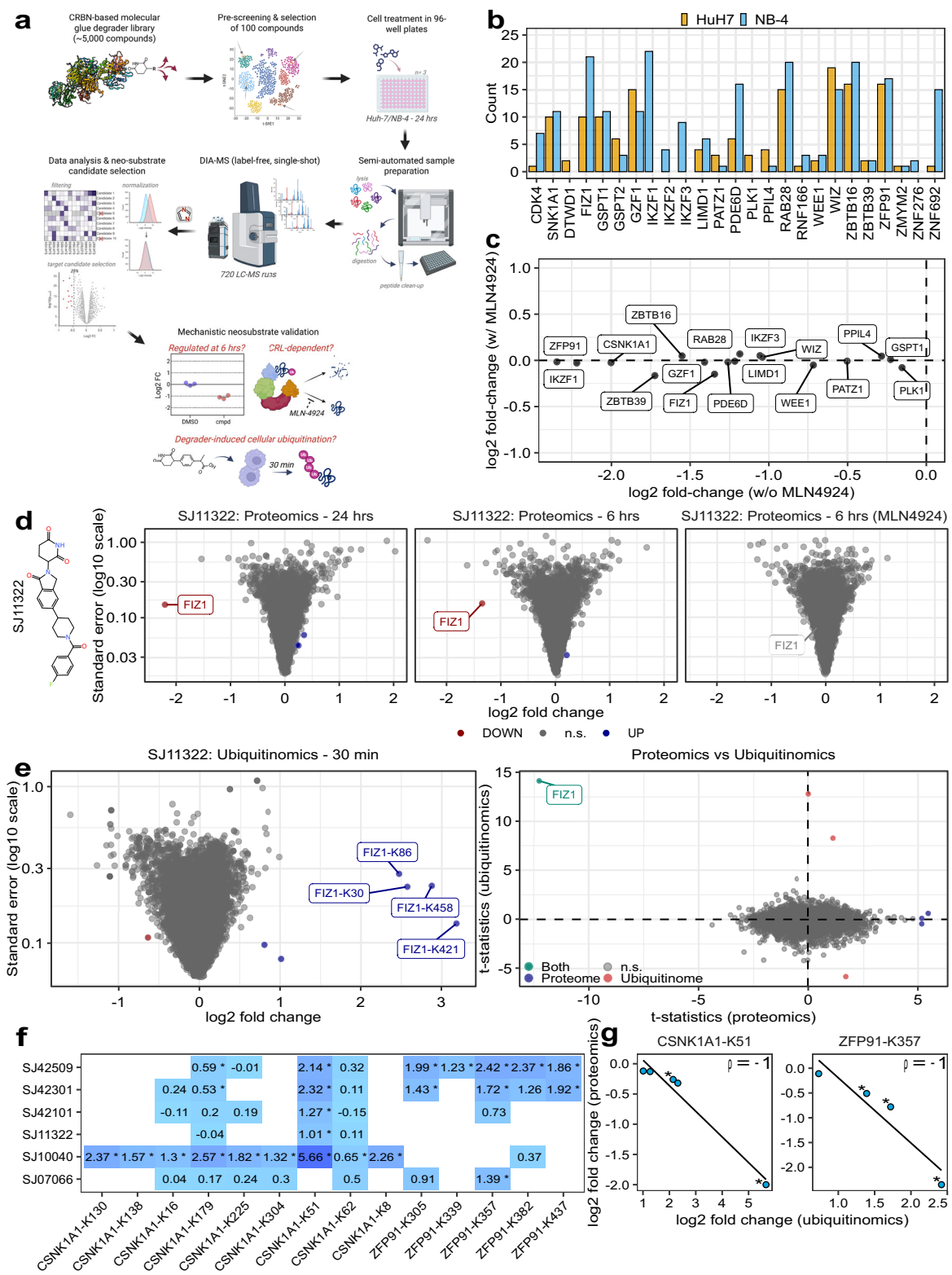
neosubstrates, we next conducted a series of global ubiquitinomics analyses[26,27]. Since drug-induced protein ubiquitination can occur within minutes[27,28], we employed a 30-minute treatment time without a proteasome inhibitor to capture ubiquitination dynamics under physiological conditions. These experiments confirmed degrader-induced ubiquitination of several previously reported neosubstrates, including LIMD1, GZF1, PPIL4, and FIZ1, thereby validating our screening strategy (Fig. 1e and Supplementary Figs. 3, 4).

Our site-specific ubiquitination analysis further enabled a detailed investigation of neosubstrate ubiquitination patterns. A key observation was the frequent occurrence of ubiquitination in the absence of detectable protein degradation, indicating that ubiquitination alone is not always sufficient to trigger proteolysis. Notably, specific lysine residues on individual neosubstrates served as priming sites for degradation, showing the strongest correlation with protein down-regulation. For instance, ubiquitination at CSNK1A-K51 emerged as a

Fig. 1 | The molecular glue degrader (MGD) proteomics screening workflow.
a Schematic of the proteomics screening workflow. A subset of 100 CRBN-based molecular glue degraders (MGDs) from a 5000-compound library was screened in Huh-7 and NB-4 cells (10 μM, 24 h) in 96-well plates. Each plate included 25 MGDs in triplicate. Proteins were quantified using Bruker timsTOF MS and processed with DIA-NN[14]. Significantly downregulated proteins (>25%) were selected for 6-h re-testing with or without MLN4924, a neddylation inhibitor. Ubiquitinomics (K-GG peptide profiling) was used to validate MLN4924-dependent neosubstrates. Created in BioRender. BioRender.com/h02z778. **b** Count of significant downregulation events (LIMMA[69], FDR = 1%) for known neosubstrates in Huh-7 or NB-4 cells after 24-h compound treatment (see Supplementary Data 2) for details. **c** Scatter plot showing suppression of MGD-induced downregulation (6 h) of known CRBN neosubstrates by MLN4924 (5 μM). **d** Volcano plots showing protein-level effects of SJ11322 (10 μM), from left to right: (i) 24 h, (ii) 6 h, and (iii) 6 h with MLN4924 (5 μM). Log2 fold-change (x-axis) and log10 standard error (y-axis) are shown. The chemical structure of SJ11322 is shown on the left side. Up- and downregulated proteins or ubiquitination sites (LIMMA[69], FDR = 1%/5%) are colored in blue and red. *P*-value adjustments were made for multiple comparisons using the Benjamini-Hochberg procedure. n.s. not significant. The chemical structure of SJ11322 is shown. **e** Left: Volcano plot of SJ11322-induced ubiquitinated peptides (30 min). Upregulated sites (LIMMA[69], FDR = 5%) are in blue, including four FIZ1 sites. Right: Correlation of proteome (x-axis) and ubiquitinome (y-axis) *t*-statistics. Significantly regulated proteins/sites are colored; turquoise highlights proteins downregulated at 24 h with increased ubiquitination at 30 min. n.s. not significant. **f** Heatmap of log2 fold-changes in ubiquitination for CSNK1A1 and ZFP91. Asterisks (*) indicate statistically significant regulations (LIMMA[69], FDR = 5%). **g** Correlation between site-specific ubiquitination−CSNK1A1-K51 (left; Spearman's ρ = −1, *p*-value = 0.02) and ZFP91-K357 (right; Spearman's ρ = −1, *p*-value = 0.08)−with corresponding 6-hour protein downregulation. Asterisks (*) indicate significant protein downregulation (LIMMA[69], FDR = 1%); linear regression line and Spearman coefficient are shown. Source Data are provided as a Source Data file.

critical marker, with only a ~4-fold increase sufficient to induce detectable protein degradation. While weaker degraders primarily promoted ubiquitination at K51 and to a lesser extent at K179, the most potent degrader (SJ10040) induced ubiquitination at seven additional sites, suggesting an additive effect on degradation efficiency. Similarly, the extent of ZFP91-K357 ubiquitination showed the strongest correlation with protein loss (Fig. 1f, g). Echoing prior observations with BRD4-BD2 site-selective ubiquitination by MZ1[28], our findings identified key lysine residues that act as a functional ubiquitination hotspot driving neosubstrate degradation in a native cellular context.

Collectively, these results highlight that the combination of our MGD library design with MS-based proteomics and ubiquitinomics can identify and validate high-quality degrader probes for poorly characterized neosubstrates and provide insights into the mechanistic regulation of intracellular neosubstrate ubiquitination.

Systematic discovery of novel CRBN neosubstrates

We next analyzed our dataset for putative novel CRBN neosubstrates, initially focusing on Huh-7 cells. Out of the 100 compounds tested at 24 h, 32 resulted in a decrease in cellular abundance of at least one protein by more than 25%, leading to a preliminary list of 84 novel neosubstrate candidates. The 32 hit compounds were retested at the 6-h time point, confirming the downregulation of 26 target candidates (by 16 compounds). UHRF1, ZNF430, ZNF644, DHX37, and CCNK were just below statistical significance or our 25%-fold change cut-off in the 24-h dataset but showed significant and robust downregulation at 6 h. We therefore included them in the follow-up experiments (Supplementary Data 3). For each neosubstrate candidate, we selected at least one representative compound and assessed CRL dependency by treating cells with MLN4924 alongside the degrader. This combination substantially attenuated the downregulation of 23 proteins (to less than 70%), supporting their classification as putative novel CRBN neosubstrates (Fig. 2a). In contrast, we also observed several CRL-independent downregulation events, such as those involving the cytochrome P450 enzyme CYP2J2 and oxysterol-binding protein-related protein 8 (OSBPL8), likely reflecting CRBN-independent off-target effects (Supplementary Fig. 5).

For further validation, we subjected the 23 CRL-dependent neosubstrate candidates to quantitative ubiquitinomics. This revealed a total of 16 novel CRBN neosubstrates, including enzymes (Lysine-specific histone demethylase 4B (KDM4B)[29]), regulators of transcription (CCR4-NOT transcription complex subunit 4 (CNOT4)[30] and the zinc finger protein ZBTB7B[31]), and tumor suppressors (Folliculin (FLCN)[32]) (Fig. 2b, c, Supplementary Fig. 6 and Supplementary Data 3).

Among the newly identified neosubstrates, we noted several members of established protein complexes, including CSNK1A1 and its interaction partners FAM83G and FAM83B, components of the CDK-activating kinase (CAK) complex (CDK7, CCNH, and MNAT1), and the CDK13-CCNK pair (Supplementary Fig. 7)[33-35]. We hypothesize that the recruitment of a single complex member to MGD-bound CRBN positions associated proteins in close spatial proximity, thereby facilitating their ubiquitination as bystander neosubstrates[36-38].

In the case of the CSNK1A1-FAM83B/G complex, CSNK1A1 is the established direct neosubstrate[38,39], and consistent with this, we did not identify any β-hairpin G-loop motifs in FAM83G or FAM83B.

Similarly, within the CAK complex, MNAT1 appears to be the direct MGD target, as indicated by its stronger downregulation and ubiquitination relative to CDK7 and CCNH. This is further supported by recent reports demonstrating CRBN recruitment of MNAT1 via a β-hairpin G-loop recognition motif, which is absent in the other CAK complex members[37,40].

We observed a similar pattern for the CDK13-CCNK pair, in which case CDK13 degradation was much more pronounced. The presence of a G-loop motif in CDK13, but not in CCNK, supports its classification as the direct CRBN neosubstrate. Notably, this mechanism diverges from previously reported CCNK degraders, which act through a drug-induced interaction of CDK12 or CDK13 with DDB1[41-43].

We identified two compounds (SJ42101 and SJ6986) that downregulated MNAT1. While SJ42101 downregulated only 13 proteins, the potent GSPT1/GSPT2 degrader SJ6986 affected thousands, obscuring direct degradation events due to secondary effects from disrupted protein biosynthesis[11,44]. To differentiate between direct target degradation and indirect GSPT1-mediated effects, we conducted global ubiquitinomics with both compounds. SJ42101 induced ubiquitination of 7 neosubstrates, whereas SJ6986 triggered the ubiquitination of GSPT1, GSPT2, their complex partner ETF1[45], and the proteins MNAT1, CDK7, RERE, GZF1, WIZ and ZBTB7B (Fig. 2d, e). This demonstrates that our integrated MS-based screening approach enables the specific extraction of primary degrader targets from complex proteomic profiles, such as those induced by GSPT1 degradation.

To assess potential cell line-specific responses of MGDs, we extended our proteomic screening efforts to NB-4 cells. While we could replicate most CRL-dependent protein downregulations identified in Huh-7 cells (e.g., KDM4B or CNOT4), some effects appeared to be cell type-specific. Notably, ZBTB7B was downregulated by SJ42101 only in Huh-7 cells, whereas SJ10040 selectively reduced levels of the ubiquitously expressed kinase CSNK1E in NB-4 cells, despite comparable expression levels in both cell lines (Supplementary Fig. 8a−c). Similarly, the KDM4B degrader SJ41564 significantly downregulated the highly expressed cytoskeletal protein vinculin (VCL) only in NB-4, even though it was ubiquitinated in both cell lines (Supplementary Fig. 8d). These findings indicate that MGDs can elicit cell-type-specific degradation profiles, even for ubiquitously expressed proteins. While the underlying mechanisms remain to be elucidated, our data highlight the value of performing proteomic MGD screens across diverse cellular contexts to uncover cell-specific neosubstrates.
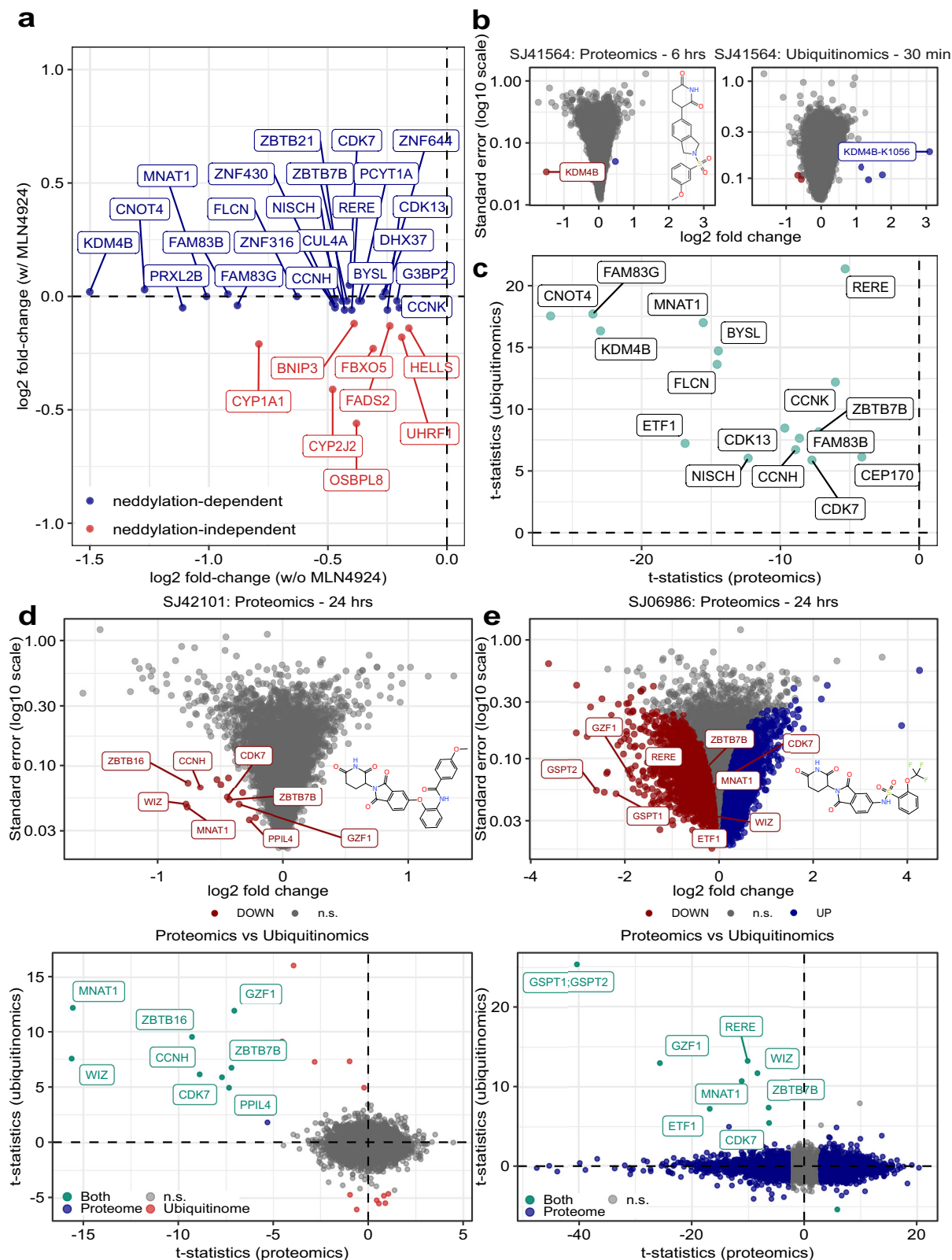
Overexpression of CRBN enhances neosubstrate identification

Our ubiquitinomics-based validation in Huh-7 cells identified 16 novel neosubstrates (Fig. 2c), and we further validated VCL as a CRBN neosubstrate in NB-4 cells. However, we did not detect compound-induced ubiquitination for the remaining 11 neosubstrate candidates. These were ZBTB21, CSNK1E, ZNF316, CUL4A, ZNF644, PRXL2B, G3BP2, ZNF430, DHX37, PCYT1A and STK38 (Supplementary Data 4).

These proteins were either expressed at low levels or exhibited only modest downregulation upon treatment, suggesting potential sensitivity limitations of our assay.

We hypothesized that increasing CRBN expression could enhance cellular CRL4^{CRBN} activity, thereby amplifying neosubstrate ubiquitination and degradation, as previously shown for substrates regulated by lenalidomide[46]. We therefore generated a HEK293 cell line with

Fig. 2 | Discovery of novel neosubstrates in Huh-7 cells. a Scatter plot illustrating newly identified CRBN neosubstrates in Huh-7 cells. The plot displays all proteins that showed significant downregulation following treatment with 10 µM MGD for 6 h (x-axis) alongside their corresponding fold-changes under co-treatment with 5 µM MLN4924 (y-axis). Proteins regulated in a neddylation-dependent manner are highlighted in blue, while those regulated in a neddylation-independent manner are indicated in red. **b** Volcano plots depicting protein (left) and ubiquitinated peptide (right) quantifications for the KDM4B degrader SJ41564 (10 µM), with $\log_2$ fold-change on the x-axis and standard error on the y-axis ($\log_{10}$ scale). Significant up- and downregulations of proteins (LIMMA[69], FDR = 1%) or ubiquitination sites (LIMMA[69], FDR = 5%) are colored in blue and red, respectively. **c** Summary of proteome (x-axis) and ubiquitinome (y-axis) t-statistic comparisons for all newly validated neosubstrates in Huh-7 cells. T-statistics for ubiquitination sites mapped to the same protein were averaged, and only significantly upregulated sites were included in the analysis. Volcano plots of protein quantifications for SJ42101 (**d**) and SJ06986 (**e**) after 24 h of treatment. Significantly up- and downregulated proteins (LIMMA[69], FDR = 1%) are colored in blue and red, respectively. The proteome (x-axis) and ubiquitinome (y-axis) t-statistic comparison plots are shown (bottom). Statistically significant up- and downregulations in the proteome (LIMMA[69], FDR = 1%) and the ubiquitinome (LIMMA[69], FDR = 5%) are colored in blue and red, respectively. P-value adjustments were made for multiple comparisons using the Benjamini-Hochberg procedure. Proteins that are both significantly downregulated after a 24-h compound treatment and harbor upregulated ubiquitination sites at 30 min of compound treatment are colored in turquoise. n.s. not significant. Source Data are provided as a Source Data file.

stable CRBN overexpression (HEK293-CRBNoe), which exhibited about eight-fold higher levels of CRBN than the parental line (Supplementary Fig. 9). Proteomic profiling of SJ10040-treated HEK293 and HEK293-CRBNoe cells revealed a markedly enhanced neosubstrate degradation in the CRBN-overexpressing background. We confirmed candidates of the primary screen (e.g., ZBTB21 and CSNK1E) and identified numerous additional target candidates, including ZNF324, ZBTB41, STK35, and CHD7 (Fig. 3a). Follow-up ubiquitinomics confirmed compound-induced ubiquitination for 13 neosubstrates, including four newly identified ones (Fig. 3b, top panel).

Proteomics combined with ubiquitinomics of the remaining seven compounds in HEK293-CRBNoe cells confirmed their enhanced response to MGDs, further validating CUL4A, ZNF316, PRXL2B, G3BP2, ZNF644, ZNF430, DHX37, and PCYT1A as novel neosubstrates (Supplementary Figs. 10, 11). Interestingly, the promiscuous degrader SJ42101 yielded about 30 neosubstrates, including many novel ones, such as the zinc finger proteins ZNF121, ZNF239, ZNF408, and ZNF507, the peptidase ZUP1, and the mRNA 3'-end processing factor CSFT2T (Fig. 3b, bottom panel).

Similar to previously reported observations, we identified ubiquitination events that are either productive (leading to protein degradation) or non-productive (not resulting in protein degradation)[47]. The non-productive events included validated neosubstrates (e.g., ZNF827 or RERE) as well as numerous potential novel CRBN targets (e.g., STK3/4, ZNF136, ZNF358, ZNF419, ZNF773, and others). These findings suggest that non-productive ubiquitination could potentially be converted into productive degradation through broader compound screening campaigns.

The systematic profiling of different MGDs by proteomics and ubiquitinomics across different cell lines allowed a cross-comparison of site-specific ubiquitination and protein degradation in different biological contexts. As for HuH-7, we confirmed CSNK1A1-K51 and ZFP91-K375 ubiquitination as priming events for protein degradation in NB-4 and in HEK293 cells. Similarly, ubiquitination of MNAT1 at K176 strongly correlated with protein downregulation across different cell lines (Fig. 3c).

Collectively, our integrated MS-based strategy revealed 50 novel neosubstrates from a set of 100 compounds, including 17 proteins without a predicted GSPT1-like G-loop, demonstrating a much broader target scope for CRBN-based degraders than previously recognized (Fig. 3d, Supplementary Fig. 12, and Supplementary Data 5).

Impact of MGD structure on degradation specificity and selectivity: structure-degradation relationship

Almost all screened compounds (98 out of 100) either contained classical IMiD core structures as present in thalidomide and lenalidomide or possessed a phenyl-glutarimide (PG) core recently introduced as an alternative CRBN-binding warhead (Fig. 4a)[17]. Our comprehensive data collection allowed us to explore correlations between MGD chemical structure and cellular degradation activities. To do that, we first grouped all compounds that degraded known or newly identified neosubstrates in Huh-7 and NB-4 cells according to whether they contained either an IMiD-like or PG core structure, followed by hierarchical clustering of protein fold-changes (i.e., MGD vs. DMSO) within both subsets. Notably, most classical IMiD targets, including IKZF1, ZFP91, CSNK1A1, GSPT1, GZF1, or RAB28, were selectively degraded by MGDs featuring IMiD-like cores. In contrast, LIMD1 and novel neosubstrates, including KDM4B or FLCN, were exclusively targeted by PG-based compounds, which also exhibited a much higher overall neosubstrate selectivity (Fig. 4b and Supplementary Fig. 13). A third category of neosubstrates included proteins such as FIZ1, ZBTB39, and the novel neosubstrate G3BP2, which were degraded to a similar extent by both PG-based and IMiD-like MGDs. However, while the IMiD-like G3BP2 degrader SJ42229 co-depleted several known IMiD targets, none of these were affected by the selective PG-based G3BP2 degrader SJ41824, further highlighting the higher selectivity of PG-based MGDs (Fig. 4c). Given the association between IMiD-induced teratogenicity and SALL4 degradation[48], we extended our analysis to the human testicular embryonal carcinoma cell line SUSA, which expresses high levels of SALL4. Strikingly, all 10 IMiD-like compounds tested induced strong downregulation of SALL4, while only 1 out of 10 PG-based compounds caused a moderate decrease (Fig. 4d).

Given their remarkable selectivity, we next focused on the in-depth characterization of the PG-based degraders of G3BP2 and KDM4B.

Characterization and chemical optimization of MGDs targeting G3BP2 and KDM4B

Given the advantage of high compound selectivity in defining starting points for further chemical optimization, we selected the PG-based degrader SJ41824 targeting G3BP2 for chemical analog testing. G3BP2 is an mRNA-binding protein that physically associates with both G3BP1 and USP10, playing a key role in protecting ribosomes from degradation under cellular stress[49]. At present, no selective G3BP2 inhibitors have been reported. To establish a structure-degradation relationship around this chemotype and potentially identify more potent degraders, we evaluated additional SJ41824 analogs in NB-4 cells by global proteomic profiling. Among these, SJ41813 caused stronger and highly selective degradation of both G3BP2 and USP10, as determined by Western blotting and proteomics (Fig. 4e and Supplementary Fig. 14a, b). Notably, SJ41813 differs from SJ41824 only by the position of fluorine atoms on the phenyl ring (3,4- vs. 2,4-difluoro), underscoring the impact of subtle structural changes on degradation efficacy[50]. CRISPR-Cas9-mediated knockout of CRBN in SK-N-BE(2)-C cells completely abrogated G3BP2 degradation by SJ41813 (Fig. 4e), confirming a CRBN-dependent mechanism.

To demonstrate ternary complex formation, we engineered a HEK293 cell line with doxycycline-inducible expression of TurboID-CRBN[51] and treated it with SJ41813. Affinity-purification followed by quantitative mass spectrometry revealed a >6-fold enrichment of G3BP2, alongside weaker enrichment of binding partners such as USP10, pointing to G3BP2 as the direct CRBN neosubstrate (Fig. 4f). Consistently,
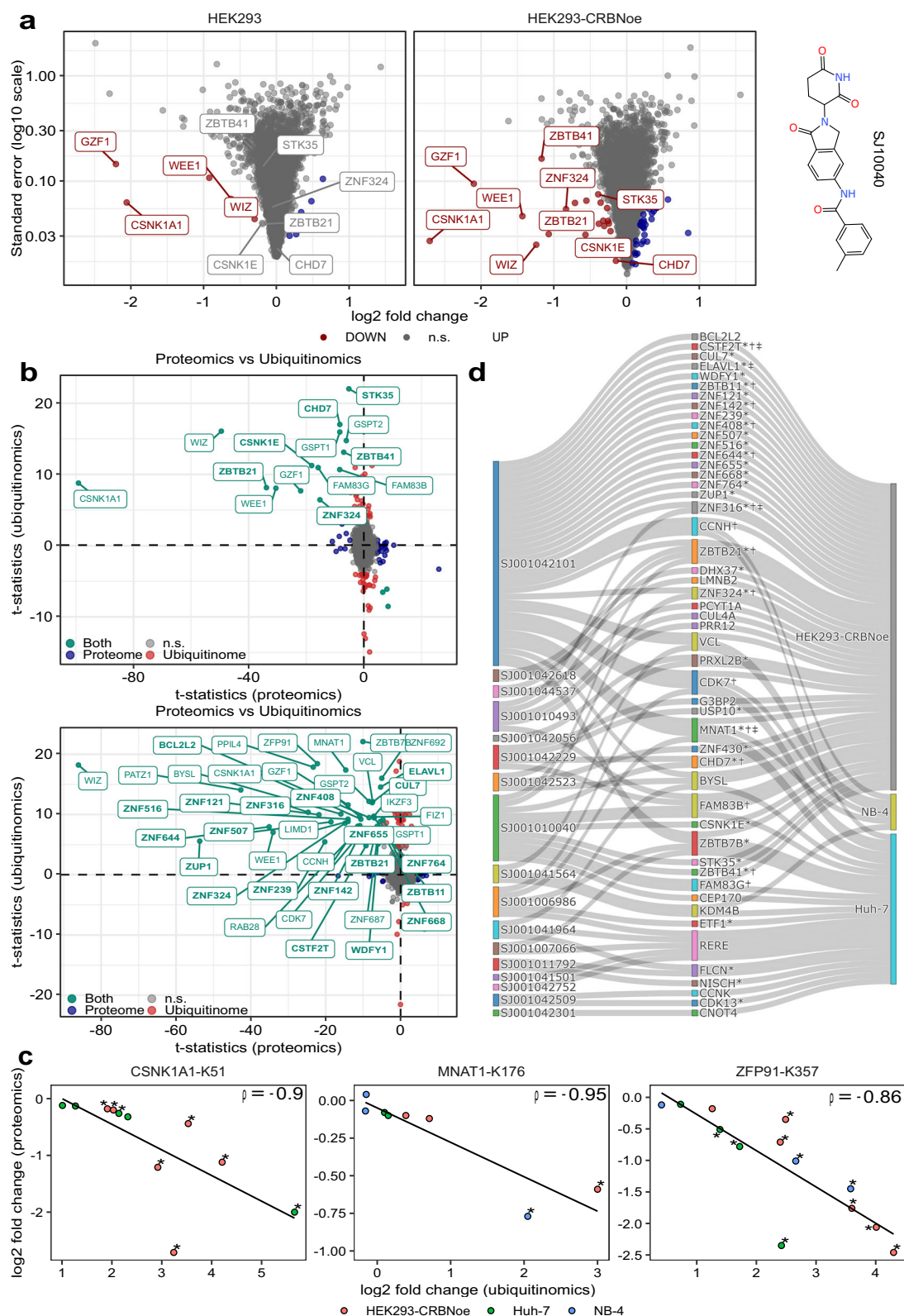
G3BP2 showed greater degradation potency ($DC_{50} = 2.2\,\mu M$) than USP10 ($DC_{50} = 10\,\mu M$) (Fig. 4g, h). Ubiquitinomics further revealed two SJ41813-induced ubiquitination sites on G3BP2 but none on USP10 in NB-4 cells (Fig. 4i), a result corroborated by enhanced G3BP2 ubiquitination in SJ41813-treated HEK293-CRBNoe cells (Supplementary Fig. 14c). Together, these findings establish G3BP2 as a bona fide CRBN neosubstrate, aligning with recent reports[52].

The second PG-based degrader selected for analog optimization was SJ41564, which induced potent and selective degradation of KDM4B. KDM4B is a histone demethylase that targets H3K9 and H3K36, which are key histone marks involved in gene regulation and chromatin organization[53,54]. It shares high sequence homology with other KDM4 family members, including KDM4A and KDM4C, which are frequently overexpressed in cancer[55]. Despite extensive efforts in

Fig. 3 | Neosubstrate discovery in HEK293-CRBNoe cells. a Volcano plots showing protein quantifications of HEK293 (left) and HEK293-CRBNoe (right) in response to the degrader compound SJ10040. The x-axis represents $\log_2$ fold change, while the y-axis shows standard error on a $\log_{10}$ scale. Both cell lines were treated with the compound for 6 h. Significantly up- and downregulated proteins, as determined by LIMMA[69] (FDR = 1%), are indicated in blue and red, respectively. The chemical structure of SJ10040 is shown on the right side. n.s. not significant. **b** Comparison plot of the t-statistics of the proteome (x-axis) and the ubiquitinome (y-axis) for the two MGDs SJ10040 (top) and SJ42101 (bottom) in HEK293-CRBNoe cells. The t-statistics of significantly upregulated ubiquitination sites mapping to the same gene were averaged. Statistically significant up- and downregulations of the proteome (LIMMA[69], FDR = 1%) and the ubiquitinome (LIMMA[69], FDR = 5%) are colored in blue and red, respectively. Proteins that were significantly downregulated after 6 h of compound treatment and exhibited upregulated ubiquitination sites at 30 min of compound treatment are highlighted in turquoise. P-value adjustments were made for multiple comparisons using the Benjamini-Hochberg procedure. Neosubstrates that were identified and validated in HEK293-CRBNoe are indicated in bold. n.s. not significant. **c** Correlation between site-specific ubiquitination−CSNK1A1-K51 (left; Spearman's $\rho = -0.9$, p-value = 0.0002), MNAT1-K176 (middle; Spearman's $\rho = -0.9$, p-value = 0.0004), and ZFP91-K357 (right; Spearman's $\rho = -0.9$, p-value = 0.0003) on the x-axis−and corresponding protein downregulation after 6 h of compound treatment (y-axis). The different colors indicate the cell line, and asterisks (*) statistically significant protein downregulation, and a best-fitting linear regression line, along with the Spearman correlation coefficient, is shown. **d** Sankey diagram summarizing all novel neosubstrates identified and validated through ubiquitinomics in Huh-7, NB-4, and HEK293-CRBNoe cells. Compounds are displayed on the left side of the diagram, and the corresponding cell lines are on the right side. Asterisks (*) denote predicted G-loop motifs, while † and ‡ proteins previously reported as CRBN binders in Refs. [40] and [37], respectively. Source Data are provided as a Source Data file.

both industry and academia[56], selective inhibitors for individual KDM4 isoforms have remained elusive, largely due to the high structural similarity of their JmjC catalytic domains[56]. SJ41564 selectively degraded KDM4B without affecting the levels of other KDM4 family members, including KDM4A, KDM4C, and KDM4D, in both NB-4 and Huh-7 cells (Fig. 5a). Interestingly, in SK-N-BE(2)-C cells, KDM4B degradation was accompanied by a modest increase in KDM4A expression, suggesting a potential compensatory response specific to this neuroblastoma cell line (Supplementary Fig. 15a). A similar mechanism has been reported in rhabdosarcoma cells, where KDM4A regulation mitigates the impact of KDM4B silencing on cell growth[57].

To confirm the CRBN-dependent mechanism of SJ41564, we compared its activity to a structurally related, inactive analog (SJ48108), featuring an N-methyl modification. As expected, only SJ41564 induced a rapid and potent degradation of KDM4B, with a DC_{50} of 36 nM and a D_{max} of 92% at 10 μM. (Fig. 5b, c, and Supplementary Fig. 15b, c). Beyond the initial four cell lines (HEK293, Huh-7, NB-4 and SK-N-BE(2)-C), SJ41564 also induced KDM4B degradation across six other cancer cell lines, highlighting its broad cellular activity (Supplementary Fig. 15d). Consistent with proteomics findings in NB-4 cells, SJ41564-induced KDM4B degradation in SK-N-BE(2)-C cells was fully blocked with the proteasomal inhibitor MG132, the NEDD8-activating enzyme inhibitor MLN4924, or the CRBN ligand lenalidomide. Moreover, KDM4B degradation was completely abolished in SK-N-BE(2)-C $CRBN^{KO}$ cells and occurred without changes in KDM4B mRNA levels, confirming a post-translational mechanism (Supplementary Fig. 15e−g). Together, these results establish that SJ41564 mediates KDM4B degradation through a CRBN- and ubiquitin−proteasome-dependent pathway.

Having established CRBN dependency, we next sought to identify the region of KDM4B responsible for engaging with CRBN-bound SJ41564. The KDM4 proteins contain several structured domains, including the JmjN and JmjC catalytic domains, as well as tandem TUDOR and PHD domains (Fig. 5d). While the JmjC domain is highly conserved among KDM4 members, the tandem TUDOR domains exhibit markedly lower sequence homology and are found only in KDM4A and C. To map the degron region, we generated a series of KDM4B protein fragments (A−F) and expressed them in SK-N-BE(2)-C cells stably expressing CRBN. Western blot analysis following incubation with SJ41564 revealed selective degradation of fragments E and F, in contrast to fragments A−D, implicating the tandem TUDOR domains in mediating CRBN-dependent degradation of KDM4B.

TurboID-based proximity labeling confirmed SJ41564-induced ternary complex formation in HEK293 cells (Fig. 5e). To further validate this interaction, we developed an AlphaScreen assay using a GST-KDM4B fragment containing the PHD and tandem TUDOR domains (PHD-DTD) and recombinant His-CRBN-DDB1. SJ41564 induced dose-dependent ternary complex formation with an EC_{50} of 4.7 μM, confirming direct interaction between the glue, CRBN, and KDM4B

(Fig. 5f). No signal was observed with N-methylated negative control compound SJ48108, consistent with its inability to bind CRBN.

Subsequent quantitative proteomics evaluation of SJ41564 analogs identified additional potent KDM4B degraders, revealing that the *meta*-position on the distal phenyl moiety is favored for cellular activity (Fig. 5g, Supplementary Fig. 16).

Strikingly, while para-substituted analogs exhibited little to no KDM4B degradation activity, several of these PG-based CRBN binders unexpectedly triggered a pronounced reduction in the cytoskeletal protein vinculin (VCL)[58]. Notably, compounds such as SJ46479 and SJ47878 reduced VCL levels by 90% within 6 h, with high selectivity in both NB-4 and Caki-1 cells (Fig. 5g, h). Further characterization of SJ46479 in Caki-1 cells revealed time-, dose-, and CRBN-dependent degradation of VCL, with a DC_{50} of 255 nM and a D_{max} of 96%, establishing it as a potent and selective VCL degrader (Supplementary Fig. 17).

Finally, proximity labeling coupled to MS analysis confirmed intracellular ternary complex formation between VCL and CRBN. In NB-4 cells, SJ46479 triggered rapid ubiquitination of over 20 lysine residues on VCL following treatment of NB-4 cells with SJ46479 (Fig. 5i, j). Structural mapping of these ubiquitination sites onto the predicted VCL protein model revealed a concentrated ubiquitination zone, offering insights into the spatial orientation of VCL within the CRBN E3 ligase complex (Supplementary Fig. 18).

To identify the specific region of VCL directly involved in the ternary complex formation, we generated Caki-1 cell lines stably overexpressing FLAG-tagged constructs of each of the five distinct VCL domains (A-E) and assessed their protein levels by immunoblotting (Supplementary Fig. 19a−c). Upon treatment with SJ46479, we observed changes only in the level of D1, while the other four constructs remained unaffected (Supplementary Fig. 19b), suggesting that the D1 domain is the one involved in the direct interaction of VCL with the neomorphic SJ46479-CRBN surface. Interestingly, while the level of D1 was markedly low in untreated cells, it was found to be significantly increased in cells treated with either SJ46479 or the proteasome inhibitor MG132 (Supplementary Fig. 19c). This suggests that, while unstable on its own due to proteasomal degradation, D1 is stabilized by the SJ46479-induced complexation with CRBN. We speculate that the three ubiquitination sites in D1 fragment (K170, K216, and K219), out of over 20 identified in the full-length protein (Fig. 5i, Supplementary Fig. 18), are not effectively ubiquitinated when in the ternary complex with SJ46479-CRBN, rendering SJ46479 incapable of inducing degradation and thereby resulting in D1 protein stabilization.

In summary, our proteomics-driven screening strategy identified highly selective PG-based degraders for G3BP2, KDM4B, and VCL. This work further highlights the profound impact of subtle chemical modifications on CRBN-based degrader specificity and demonstrates the potential of systematic MGD discovery to uncover potent and selective degraders of previously unreported CRBN neosubstrates.
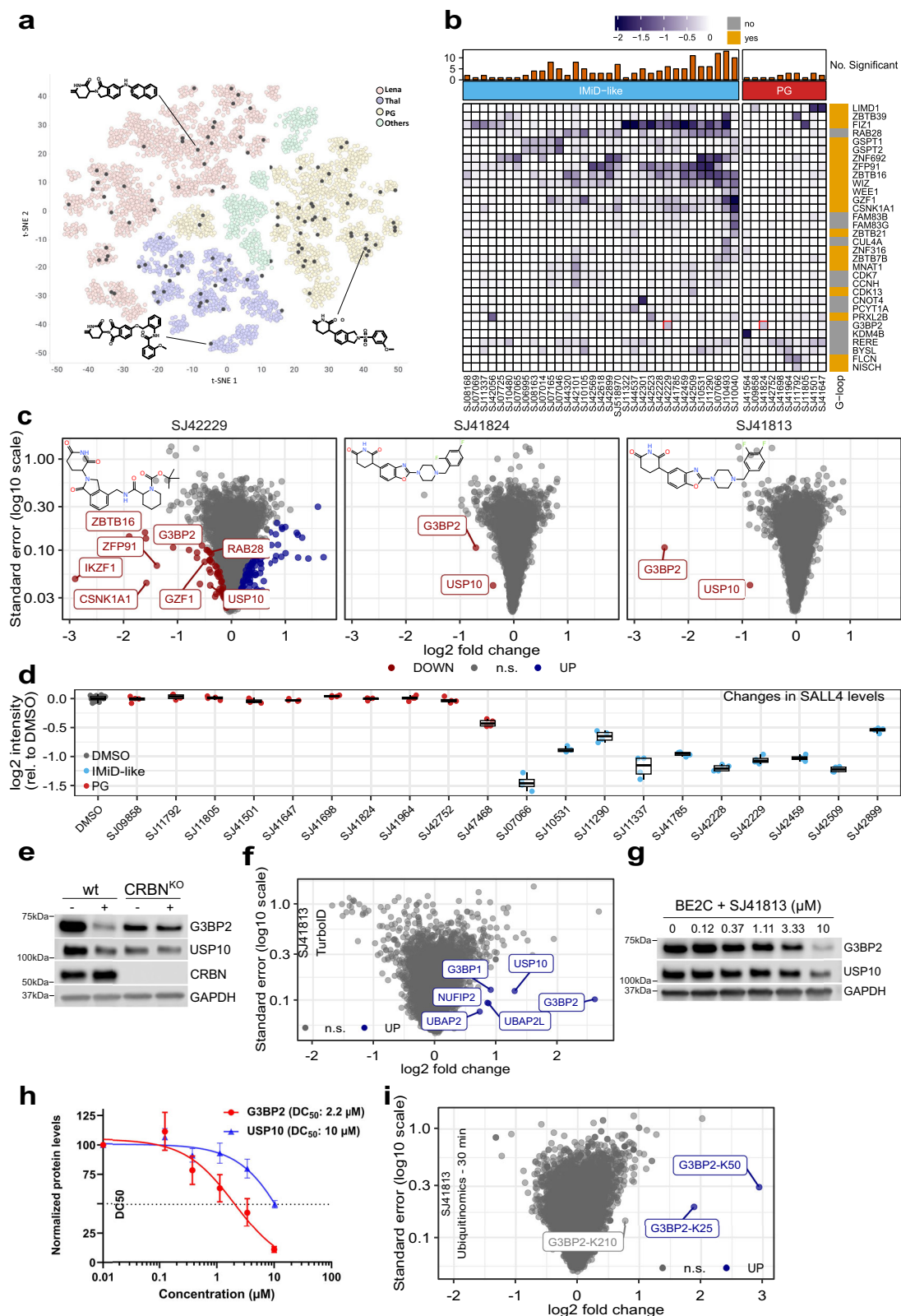
Discussion

In this study, we present an unbiased and highly sensitive screening workflow based on MS-based proteomics for the discovery of MGDs and their neosubstrates in intact cells. Our platform integrates compound profiling across multiple time points and cell lines, incorporates neddylation inhibition to distinguish direct and CRBN-dependent protein degradation events, and employs ubiquitinomics for rigorous

target validation. By screening a chemically diverse set of 100 CRBN ligands, we identified and validated 50 previously unreported neosubstrates. Notably, many of these had been implicated in ternary complex formation in prior biochemical or cell-based assays, underscoring the robustness and biological relevance of our approach[9,36,37,40].

To enhance the sensitivity for neosubstrate identification, we utilized HEK293 cells overexpressing CRBN, which enabled us to

Fig. 4 | Structure-degradation relationship analysis of screened MGDs. a t-SNE plot of MGDs clustered by core structure: lenalidomide (Lena), thalidomide (Thal), and phenyl-glutarimide (PG). Each dot represents a compound; black dots indicate the 100 analogs selected for proteomics. Representative core structures are shown. **b** Heat map of $\log_2$ fold-changes (MGD vs. DMSO) for known and novel neosubstrates in Huh-7 cells. Compounds are grouped by IMiD-like or PG-based cores. The top bar chart shows the number of significantly downregulated neosubstrates per compound. Red boxes highlight G3BP2 degradation by SJ42229 and SJ41824. Proteins with predicted G-loop motifs are indicated. **c** Volcano plots depicting protein quantifications for the G3BP2 SJ42229 (IMiD-like), SJ41824 and SJ41813 (PG-based) in NB-4 cells (10 μM, 24 h). The x-axis shows $\log_2$ fold-changes, and the standard errors are plotted on the y-axis ($\log_{10}$ scale). Significant changes (LIMMA[69], FDR = 1%) are in red (down) and blue (up). IMiD-derived neosubstrates are highlighted for SJ42229. The compound structures are shown. n.s. not significant. **d** MS quantified SALL4 levels in SUSA cells after treatment with IMiD-like (blue) and PG-based (red) compounds (10 μM, 24 h). Box plots represent $\log_2$-transformed intensity values for

four biological replicates per compound, with 15 DMSO-treated samples included as controls. Horizontal lines indicate the median (bold) and interquartile range (thin). **e** Western blot analysis of the indicated proteins in SK-N-BE(2)-C wild-type and CRBN knockout (CRBN[KO]) cells treated with SJ41813 (10 μM, 24 h). Shown are the results of one experiment. **f** Volcano plot of biotinylated proteins from TurboID-CRBN HEK293 cells treated with SJ41813, showing $\log_2$ fold-changes (x-axis) and $\log_{10}$ standard error (y-axis). Significantly enriched proteins (LIMMA[69], FDR = 1%, n = 3) are labeled in blue. n.s. not significant. **g** Immunoblots for G3BP2 and USP10 in SK-N-BE(2)-C cells treated with increasing doses (in μM) of SJ41813 (24 h). Blots are representative of three independent experiments. **h** Quantification of G3BP2 and USP10 blots from (**g**). DC_{50} values were calculated from band intensities (mean ± S.D., n = 3) and normalized to DMSO controls. **i** Volcano plot of ubiquitinated peptides in NB-4 cells treated with SJ41813 (30 min). Significantly upregulated peptides (LIMMA[69], FDR = 5%; n = 4) are in blue; G3BP2 sites are highlighted. n.s. not significant. Source Data are provided as a Source Data file.

validate weakly degraded neosubstrates such as ZBTB21 and CSNK1E, initially detected in Huh-7 and NB-4 cells. We anticipate that extending MGD screening to a biologically diverse panel of CRBN-overexpressing cell lines will further broaden the neosubstrate landscape of CRBN-based degraders. Interestingly, we detected cell-type-specific degradation of ubiquitously expressed proteins across the profiled cell lines. This differential degradation did not correlate with CRBN or neosubstrate expression levels, suggesting that additional factors, such as post-translational modifications (PTMs), subcellular localization, or cell-type-specific expression of accessory proteins within the ubiquitin-proteasome pathway, may influence neosubstrate engagement and degradation efficiency.

Beyond neosubstrate identification and validation, our integrated proteomics screening workflow yields high-quality datasets that can inform subsequent chemical optimization efforts[40,59]. For example, we identified SJ41824 as a selective degrader of G3BP2, a Ras−GAP SH3 domain binding protein implicated in stress granule formation and the pathogenesis of breast and prostate cancers[60,61]. As no inhibitors targeting G3BP2 have been previously reported, we synthesized and profiled a focused set of SJ41824 analogs using our proteomics platform. This structure-degradation relationship analysis led to the discovery of SJ41813, a closely related regioisomer with enhanced G3BP2 degradation potency (DC_{50} = 2.8 μM). USP10 was the only other protein regulated by SJ41813, which, according to our validation experiments, is a bystander rather than a direct neosubstrate.

Another promising hit from our screening set was SJ41564, a potent and selective degrader of KDM4B. KDM4B is a member of the histone demethylase gene family and has long been considered an attractive target in cancer drug discovery. However, the development of selective KDM4B inhibitors has proven challenging, largely due to the conserved nature of the catalytic domain and the need to compete with the abundant cofactor 2-oxoglutarate[56]. Remarkably, SJ41564 robustly induces CRBN-dependent degradation of KDM4B in NB-4 cells, with a DC_{50} of 36 nM and a D_{max} of 92%, while sparing all other ~9000 quantified proteins. Domain mapping experiments using a series of Flag-tagged KDM4B truncation constructs identified the less conserved double Tudor domains as critical for degradation, potentially explaining the exceptional selectivity of SJ41564.

Further proteomic profiling of SJ41564 analogs uncovered not only additional potent KDM4B degraders but highly selective degraders of the cytoskeletal vinculin (VCL), exemplified by SJ46479 (VCL DC_{50} = 255 nM; D_{max} = 96%). These findings align well with our broader observation that molecular glue degraders often exhibit steep structure-degradation relationships, highlighting that subtle chemical modifications can have a strong impact on neosubstrate engagement.

In summary, our unbiased high-throughput proteomics screening approach led to the discovery of several exquisitely potent, selective, and structurally distinct phenyl glutarimide-based degraders of

G3BP2, KDM4B, and VCL proteins. Notably, none of these newly identified neosubstrates contain the classical G-loop degron motif, suggesting that the scope of the CRBN-degradable proteome extends well beyond that defined by IMiD substrates. While the precise structural features governing this expanded neosubstrate recognition remain to be elucidated, our findings provide a compelling rationale for proteomics-driven screening of diverse compound libraries built on novel scaffolds. Such efforts hold significant promise for uncovering previously inaccessible targets within the disease-relevant and historically undruggable protein target space.

Methods
Reagents
MLN4924, bortezomib, 2-chloroacetamide, tris(2-carboxyethyl)phosphine hydrochloride (TCEP), sodium deoxycholate, Biotin, Na_2HPO_4, 3-(N-morpholino)propanesulfonic acid (MOPS), Tris(hydroxymethyl)-aminomethane, trifluoroacetic acid, sodium chloride, formic acid, and acetonitrile were from Merck. MG132 (Cat# HY-13259) and Lenalidomide (Cat# HY-A0003) were purchased from MedChem Express (MCE). Protease inhibitor mix from ThermoFisher Scientific (A32955). Trypsin from Promega. PTMScan® HS Ubiquitin/SUMO Remnant Motif (K-ε-GG) Kit (#59322) from Cell Signaling Technology.

Cell culture, drug treatments, and cell lysis (Proteomics)
Huh-7, NB-4, HEK293T, and HEK293 cells were from Cytion. SUSA from DSMZ. Huh-7, HEK293T, and HEK293 cells were cultured in DMEM (VWR) supplemented with 10% FCS (Thermo Fisher Scientific). NB-4 cells were grown in RPMI (VWR) and 10% FCS. RH4 and RH30 cell lines were provided by Dr. Gerald Grosveld at St Jude. The SK-N-BE(2)-C (BE(2)-C) (Cat# CRL-2268), Rh30, Kasumi-1 (Cat# CRL-2724), and Caki-1 (Cat# HTB-46) cell lines were obtained from ATCC. The SIMA (Cat# ACC 164), EW-8 (Cat# ACC 493), and SKNO-1 (Cat# ACC 690) cell lines were obtained from DSMZ. SK-N-BE(2)-C, SIMA, Rh30, Rh4, EW-8, and SKNO-1 cells were cultured in RPMI 1640 (Corning, Cat# 10040CM) supplemented with 10% fetal bovine serum (Gibco, Cat# A5256701) and 1% penicillin/streptomycin (Gibco, Cat# 15140122). The Kasumi-1 cells were cultured in RPMI-1640 Medium supplemented with 20% fetal bovine serum and 1% penicillin/streptomycin. The Caki-1 cells were cultured in McCoy's 5a Medium (ATCC, Cat# 30-2007) supplemented with 10% fetal bovine serum and 1% penicillin/streptomycin. All compounds were dissolved in DMSO to generate a 1000x stock solution. Compounds were plated in 96-well plates according to a randomized layout using an Opentrons OT-2. 25 compounds were allocated on each plate (in triplicate), along with 15 DMSO controls. Cells were treated for the specified amount of time, washed with PBS, and harvested using iST lysis buffer (PreOmics). The lysates were heated to 95 °C for 10 min while shaking in a Thermomixer (Eppendorf). The rest of the workflow (tryptic digestion and
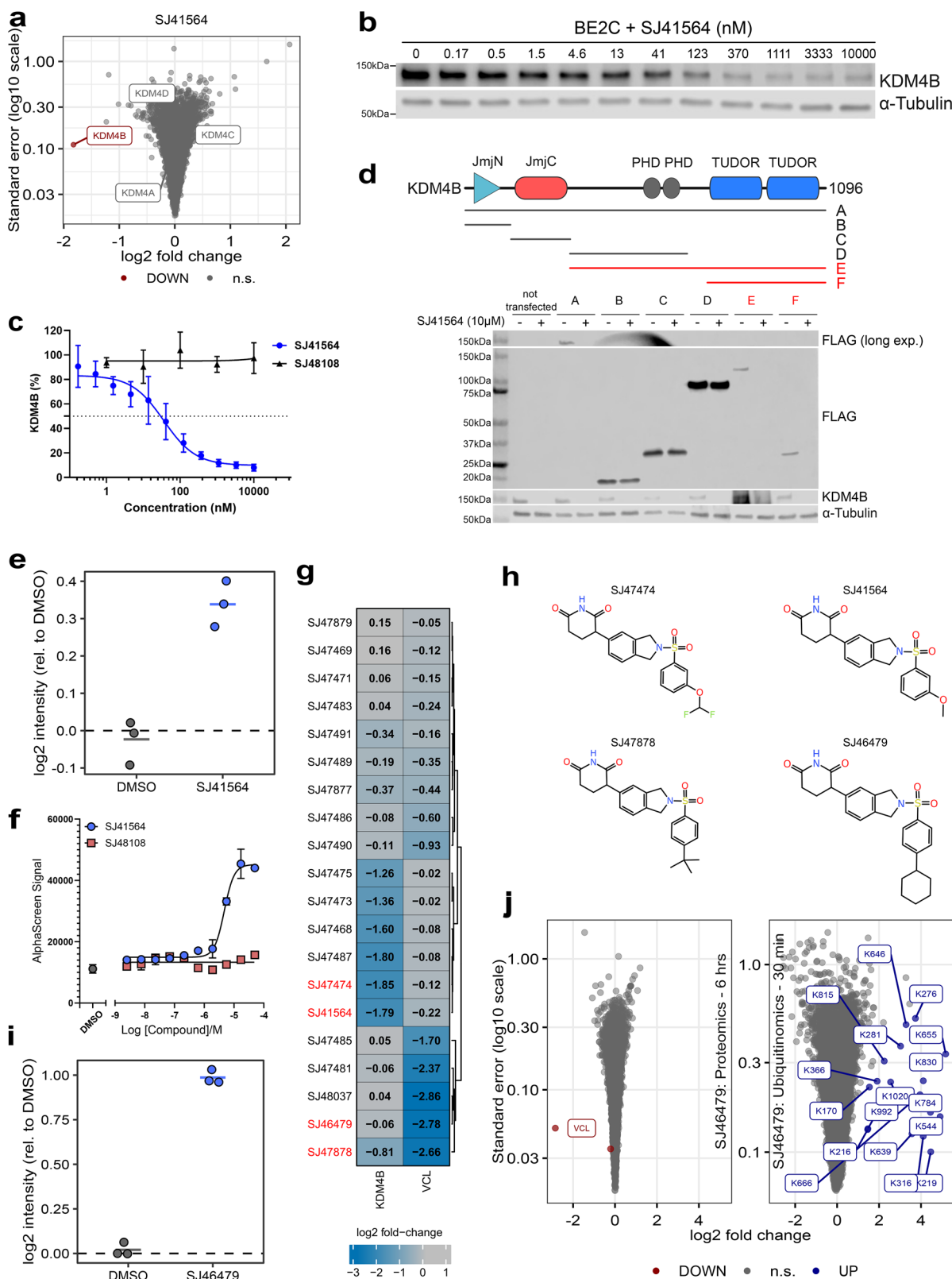
desalting of peptides) was performed according to the manufacturer's instructions.

Ubiquitinomics sample preparation
Cell treatment and sample preparation were done according to our recently established protocol with a few modifications[27]. In brief, cells (four replicates for both DMSO and compound treatments) were

cultured in 6-well plates and treated for 30 min with the specified compounds, followed by lysis with SDC buffer. Protein concentrations were determined using the BCA assay (Merck-Millipore), and the proteins were digested overnight at 37 °C using a 100:1 protein:trypsin ratio (Promega). After digestion, immunoprecipitation (IP) buffer (50 mM MOPS pH 7.2, 10 mM Na_2HPO_4, 50 mM NaCl) was added to the samples together with K-GG antibody-bead conjugate, followed by a

Fig. 5 | In-depth characterization of KDM4B and VCL as CRBN neosubstrates.
a Volcano plot of the proteome from SJ41564-treated NB-4 cells (6 h). $\log_2$ fold-change (x-axis) and $\log_{10}$ standard error (y-axis) are shown. KDM4 family members are highlighted; KDM4B is significantly downregulated (red, LIMMA[69], FDR = 1%). n.s. not significant. **b** Immunoblots of KDM4B and α-tubulin in SK-N-BE(2)-C cells treated with increasing concentrations of SJ41564 (nM, 24 h). Representative of three experiments. **c** Quantification of KDM4B levels from (**b**). The N-methylated negative control SJ48108 was included. DC_{50} values were calculated from band intensities (mean ± S.D., $n = 3$), normalized to DMSO. **d** Top: Schematic of KDM4B protein architecture and truncated fragments (A–F). Bottom: Immunoblots of FLAG-tagged KDM4B fragments in CRBN-overexpressing SK-N-BE(2)-C cells treated with SJ41564 (10 μM, 24 h), shown from one experiment. Fragments E and F are labeled in red and indicate degradation by SJ41564. **e** MS quantification of KDM4B in HEK293-TurboID-CRBN cells treated with bortezomib (0.5 μM) or SJ41564 + bortezomib (120 min). KDM4B was significantly enriched (LIMMA[69], FDR = 1%, n = 3

per condition). **f** AlphaScreen assay showing dose-dependent ternary complex formation between CRBN–DDB1 and KDM4B (PHD–DTD) upon SJ41564 treatment. $EC_{50} = 4.7$ μM. No signal was observed with the negative control SJ48108. DMSO controls are shown in gray. Data represent mean ± S.D. of three technical replicates. **g** Heat map of $\log_2$ fold-changes (vs. DMSO) for KDM4B and VCL in response to various MGD compounds by global proteomics. **h** Chemical structures of selected KDM4B and VCL degraders. **i** MS quantification of VCL in HEK293-TurboID-CRBN cells treated with bortezomib or SJ41564 + bortezomib (120 min, $n = 3$). VCL was significantly enriched (LIMMA[69], FDR = 1%, $n = 3$ per condition). **j** Volcano plots of proteome (6 h) and ubiquitinome (30 min) in NB-4 cells treated with SJ46479. Significantly regulated proteins (LIMMA[69], FDR = 1%) and ubiquitinated peptides (LIMMA[69], FDR = 5%) are shown in red (down) and blue (up). VCL ubiquitination sites are highlighted. n.s. not significant. Source Data are provided as a Source Data file.

2 h incubation on a rotor wheel. Beads washing and peptide elution was performed according to the manufacturer's instructions. The peptide eluate was desalted using in-house prepared, 200 μl two-plug C18 StageTips (3 M EMPORE™)[62].

Enrichment of biotinylated proteins (TurboID-MS)
After inducing the expression of TurboID-CRBN overnight using 100 ng/ml of doxycycline, the cells were treated with the indicated degrader compounds for 2 h (in the presence of 50 mM biotin and 0.5 μM bortezomib). Cells were lysed with cold RIPA buffer (1% NP-40, 0.5% SDC, 0.1% SDS, 50 mM Tris-HCl pH = 7.5, 150 mM NaCl, freshly supplemented with Protease inhibitor mix (Pierce)) and the lysates were cleared by centrifugation (20,000 g, 10 min). 10 μl of MagReSyn® Streptavidin (Resyn Biosciences) was added to the samples, followed by 1 h incubation on a rotor wheel. Beads were washed 5 times with RIPA buffer and proteins subsequently eluted using UDM (n-Undecyl-Beta-Maltoside, Anatrace) lysis buffer (0.05% UDM, 75 mM Tris-HCl pH 8.5, 40 mM CAA, 10 mM TCEP). The lysates were incubated at 90 °C for 10 min, followed by overnight protein digestion at 37 °C using trypsin. The peptides were desalted using in-house prepared, 200 μl two-plug C18 StageTips (3 M EMPORE™) and resuspended in 0.1% formic acid before MS analysis.

LC-MS/MS measurements
Peptides were loaded on 35 cm reversed-phase columns (75 μm inner diameter, packed in-house with C_{18}-AQ 1.9 μm resin [ReproSil-Pur®, Dr. Maisch GmbH]). The column temperature was maintained at 55 °C using a column oven. Either an EASY-nLC 1200 or a Vanquish Neo system (both ThermoFisher) was directly coupled online with the mass spectrometer (timsTOF pro2, HT or Ultra2, Bruker) via a nano-electrospray source. The LC flow rate was 300 nl/min, and the complete gradient was 60 min (proteomics) or 45 min (ubiquitinomics). Data acquisition was done using diaPASEF[18] or slicePASEF[63] (for ubiquitinomics) methods. The diaPASEF method consisted of a 24 × 2 acquisition scheme (ion mobility (IM) range from 0.65 to 1.35 and m/z range from 300 to 1500) and was generated with py_diAID[64].

Plasmids and cloning
pCMV-FLAG-KDM4B (1–1096), pCMV-FLAG-KDM4B (1–130), pCMV-FLAG-KDM4B (130–356), pCMV-FLAG-KDM4B (336–916), pCMV-FLAG-KDM4B (336–1096), and pCMV-FLAG-KDM4B (917–1096) were produced by cloning the truncated KDM4B fragments individually into the pCMV vector[65].

Generation of stable cell lines
The plasmid vectors for stable cell line generation (CRBN and TurboID-CRBN) were from VectorBuilder. The plasmid vectors pGenlenti-FLAG-VCL-A (1–252), pGenlenti-FLAG-VCL-B (253–485), pGenlenti-FLAG-VCL-C (486–717), pGenlenti-FLAG-VCL-D (718–835), and pGenlenti-FLAG-

VCL-E (836–1066) were from GenScript. The plasmid vector pLC-Flag-CRBN-P2A-Hygro for the generation of a stable BE2C cell line overexpressing CRBN was a gift from Eva Gottwein (Addgene plasmid #124303). The plasmid vector lentiCRISPR v2 puro - CRBN (#1), used for generating the BE2C cell line with CRBN knockout, was a gift from Günter Schneider (Addgene plasmid # 166240)[66]. HEK293 cells with stable gene overexpression were generated by lentiviral-mediated infection of cells according to published protocols[67]. In brief, HEK293T cells were co-transfected with psPAX2, pMD2.G, pRSV-Rev, and a lentiviral construct for CRBN expression under the control of an EF1A promoter. The supernatant was harvested after 48 h of cell transfection and passed through a 0.45 μm filter. HEK293 cells were infected with the supernatant for 24 h, followed by selection of transduced cells with puromycin (1 μg/ml). CRBN overexpression was verified by MS-based proteome profiling. HEK293-TurboID-CRBN cells were generated using the PiggyBAC system. Cells were co-transfected with a vector expressing the PiggyBAC transposase and a second vector expressing both TurboID-CRBN (tetracycline-inducible) and rtTA/tTS (Reverse tetracycline-responsive transcriptional activator M2/Tetracycline transcriptional silencer), including a puromycin selection marker. Cells stably transfected with the construct were selected with 1 μg/ml puromycin, and doxycycline-dependent expression of TurboID-CRBN was verified by mass spectrometry.

Transfection of KDM4B plasmids
FLAG-tagged constructs of different KDM4B fragments were transfected into SK-N-BE(2)-C cells using Lipofectamine 3000 Transfection Reagent (Thermo Fischer Scientific, Cat# L3000008). Briefly, on day 1, 1×10^5 cells were seeded in a single well of a 6-well plate. On day 2, cells were transfected with 2.5 μg of DNA according to the manufacturer's instructions. On day 3, the transfection medium was replaced with fresh medium containing 10 μM of SJ41564. On day 4, the cells were harvested for western blot analysis after 24 h of treatment.

Total RNA extraction, cDNA synthesis, and RT-qPCR
Total RNA was extracted from cells and tumor tissues using the RNeasy Mini Kit (Qiagen, Cat # 74106) according to the manufacturer's instructions. After extraction, 0.5–1 μg of total RNA cDNA was used to synthesize cDNA using SuperScript IV First-Strand Synthesis System (Invitrogen, Cat # 18091050) according to the manufacturer's instructions. RT-qPCR was performed using SYBR Green PCR Master Mix (Applied Biosystems, Cat # 4367660) and the 7500 Real-Time PCR System (Applied Biosystems). The relative expression of each gene was normalized to GAPDH mRNA using the ΔΔCT method. The sequences of primers used are listed below.

KDM4B-F: TCACCAGCCACATCTACCAG
KDM4B-R: GATGTCCCCACGCTTCAC
GAPDH-F: AACGGGAAGCTTGTCATCAATGGAAA
GAPDH-R: GCATCAGCAGAGGGGGCAGAG

Antibodies and Western blot

Cells were lysed on ice using a lysis buffer (0.1 M Tris-HCl, pH 6.8, 200 mM dithiothreitol, 0.01% bromophenol blue, 4% sodium dodecyl sulfate, and 20% glycerol). Samples were sonicated at 4 °C for 10 s, and then boiled at 95 °C for 10 min. Cell lysates were separated on a 4–15% precast polyacrylamide gel (Bio-Rad, Cat # 4568086) and transferred to PVDF membranes (Bio-Rad, Cat # 1704272) pre-activated with methanol. Membranes were blocked in a solution of 5% milk in PBST buffer (0.1% TWEEN in PBS) and incubated for 1 h at room temperature, and incubated overnight with primary antibodies at 4 °C under gentle horizontal shaking. The next day, membranes were washed with PBST buffer and incubated with anti-mouse or anti-rabbit HRP-conjugated secondary antibodies (1:5,000). Membranes were washed with PBST buffer, incubated with SuperSignal West Pico PLUS Chemiluminescent Substrate (ThermoFisher, Cat # 34580), and developed using an Odyssey Fc Imaging System (LI-COR Corp.). Blots were analyzed using Image Studio 6.0 (LI-COR Biotech). Antibodies and working concentrations are provided within the Source Data file.

KDM4B protein construct and AlphaScreen assay

GST-KDM4B(PHD-DTD). For AlphaScreen assay development, a KDM4B plant homeodomain-double Tudor domain (PHD-DTD) construct was designed comprising residues P729–P1031, with an N-terminal GST tag connected via a 'DGGSGSG' linker. The codon-optimized KDM4B(PHD-DTD) gene fragment was synthesized, cloned into the pET30a(+) vector for E. coli expression, and the protein was subsequently produced by Genscript. The final storage buffer for the purified protein contained 50 mM Tris-HCl, 150 mM NaCl, 10% glycerol, pH 8.0.

Ternary Complex Assay (KDM4B(PHD-DTD)/CRBN-DDB1). His-tagged CRBN-DDB1 protein was prepared following the procedure reported by Matyskiela et al.[44]. All reagents were diluted in assay buffer comprising 1× PBS, 0.1% BSA, and 0.05% Tween 20. An ECHO 650 (Labcyte Inc.) acoustic dispenser was used to generate a 10-point dilution curve from DMSO stocks of the compounds directly into a 384-well OptiPlate (PerkinElmer, cat# 6007290), giving a final DMSO concentration of 0.1%. The assay mixture contained 200 nM His-tagged CRBN-DDB1 and 50 nM GST-tagged KDM4B(PHD-DTD). AlphaScreen glutathione-coated donor and AlphaScreen nickel chelate acceptor beads were purchased from PerkinElmer (cat# 6765300 and 6760141, respectively). Briefly, to a 384-well OptiPlate containing 5× compound in triplicate was added 5 μL of a 5× solution of His-CRBN-DDB1 and GST-KDM4B(PHD-DTD) and then incubated at room temperature (rt) for 1 h. After incubation, 10 μL nickel chelate acceptor (20 μg/mL final concentration) and 10 μL glutathione donor beads (20 μg/mL final concentration) were added under subdued lighting. The plate was sealed and mixed on a MixMate (eppendorf) for 1 h at rt, and then luminescence detection was collected on an Envision plate reader (PerkinElmer). A sigmoidal curve was used to fit the data using GraphPad Prism software (v10.3.1).

Raw data processing

Western blot results were analyzed using Licor Image Studio 6.0 (LI-COR Biotech). RT-PCR and DC50 figures were generated using GraphPad Prism version 10 (GraphPad Software). MS raw files were analyzed using DIA-NN[14]. Proteomics raw files were processed with v1.8.2beta9 or 1.9.1 (chemical analog testing), and ubiquitinomics raw data was processed with v1.8.2beta27. Reviewed UniProt entries (human, SwissProt 10-2022 [9606]) were used as a protein sequence database for DIA-NN searches. One missed cleavage, a maximum of one variable modification (Oxidation of methionines), and N-terminal excision of methionine were allowed. Carbamidomethylation of

cysteines was set as a fixed modification, and K-GG (UniMod: 121) was added in case of ubiquitinomics. All data processings were carried out using library-free analysis mode in DIA-NN. --tims-scan was added as an additional command in case of ubiquitinomics.

Statistical data analysis

DIA-NN outputs were further processed with R. Peptide precursor quantifications with missing values in more than 50% of samples, or <33% of the DMSO-treated samples (for proteomics, <25% of compound-treated samples in case of ubiquitinomics) were discarded. Protein abundances were calculated using both precursor and fragment ion intensities; K-GG peptide abundances were calculated based on precursor ion intensity levels using the MaxLFQ algorithm[68], as implemented in the DIA-NN R package (https://github.com/vdemichev/diann-rpackage/). Complete missing cases in any of the conditions tested were rescued by accepting low-quality precursors (i.e., q-value > 0.01), where possible. K-GG peptide to site mapping was done using reviewed entries of the human UniProt database (SwissProt, release 10-2022). The protein (or peptide) intensities were normalized by median scaling and corrected for variance drift over time (if present) using the principal components (derived from principal component analysis (PCA)) belonging to DMSO samples. Subsequently, protein (or peptide) intensities were subjected to statistical testing with variance and log fold-change moderation using LIMMA[69]. p-values corrected for multiple testing were used to assess significance for proteomics (q-value < 0.01) and ubiquitinomics (q-value < 0.05). For comparing proteome and ubiquitinome data, identifications were mapped at the gene level.

Identification of G-loop motifs

G-loop motifs were identified by structural comparison with the G-loop of GSPT1. Structural data for the human proteome were obtained from models predicted by AlphaFold[70,71]. From these models, all possible 8-amino acid segments containing glycine at the sixth position were extracted. Each of these candidate sequences was structurally superimposed on the G-loop of GSPT1, and the root mean square deviation (RMSD) was calculated. Sequences with RMSD ≤ 1.0 Å were considered structurally similar to the GSPT1 G-loop and categorized as G-loop motifs. To assess the structural accessibility of the identified G-loop motifs, the surface exposure of individual amino acids within each loop was calculated using the pPSE metric (prediction-aware part-sphere exposure) as previously described[24]. The median value of surface exposure was calculated for each loop, and loops with a median pPSE value greater than 5 were excluded from further analysis to prioritize structurally accessible motifs.

General chemistry methods and materials

See Supplementary Information for chemical synthesis of compounds.

Reporting summary

Further information on research design is available in the Nature Portfolio Reporting Summary linked to this article.

Data availability

The mass spectrometry proteomics raw data generated in this study have been deposited in the MassIVE repository (https://massive.ucsd.edu/) and can be accessed via proteome exchange with accession code PXD059111. DIA-NN is freely available for download at https://www.github.com/vdemichev/diann. Source data are provided with this paper.

References

1. Schapira, M., Calabrese, M. F., Bullock, A. N. & Crews, C. M. Targeted protein degradation: expanding the toolbox. *Nat. Rev. Drug Discov.* **18**, 949–963 (2019).

2. Nalawansha, D. A. & Crews, C. M. PROTACs: an emerging therapeutic modality in precision medicine. *Cell Chem. Biol.* **27**, 998–1014 (2020).

3. Geiger, T. M., Schäfer, S. C., Dreizler, J. K., Walz, M. & Hausch, F. Clues to molecular glues. *Curr. Res. Chem. Biol.* **2**, 100018 (2022).

4. Moreau, P., Attal, M. & Facon, T. Frontline therapy of multiple myeloma. *Blood* **125**, 3076–3084 (2015).

5. Ito, T. et al. Identification of a primary target of thalidomide teratogenicity. *Science* **327**, 1345–1350 (2010).

6. Lu, G. et al. The myeloma drug lenalidomide promotes the cereblon-dependent destruction of Ikaros proteins. *Science* **343**, 305 (2014).

7. Krönke, J. et al. Lenalidomide causes selective degradation of IKZF1 and IKZF3 in multiple myeloma cells. *Science* **343**, 301–305 (2014).

8. Chamberlain, P. P. et al. Structure of the human Cereblon–DDB1–lenalidomide complex reveals basis for responsiveness to thalidomide analogs. *Nat. Struct. Mol. Biol.* **21**, 803–809 (2014).

9. Sievers, Q. L. et al. Defining the human C2H2 zinc finger degrome targeted by thalidomide analogs through CRBN. *Science* **362**, eaat0572 (2018).

10. Nishiguchi, G. et al. Identification of potent, selective, and orally bioavailable small-molecule GSPT1/2 degraders from a focused library of cereblon modulators. *J. Med. Chem.* **64**, 7296–7311 (2021).

11. Chang, Y. et al. The orally bioavailable GSPT1/2 degrader SJ6986 exhibits in vivo efficacy in acute lymphoblastic leukemia. *Blood* **142**, 629–642 (2023).

12. Nishiguchi, G. et al. Structure-activity relationship of potent, selective, and orally bioavailable molecular glue degraders of CK1α. *ACS Med. Chem. Lett.* https://doi.org/10.1021/acsmedchemlett.4c00250 (2024).

13. Nishiguchi, G. et al. Selective CK1α degraders exert antiproliferative activity against a broad range of human cancer cell lines. *Nat. Commun.* **15**, 1–17 (2024).

14. Demichev, V., Messner, C. B., Vernardis, S. I., Lilley, K. S. & Ralser, M. DIA-NN: neural networks and interference correction enable deep proteome coverage in high throughput. *Nat. Methods* https://doi.org/10.1038/s41592-019-0638-x (2020).

15. Guzman, U. H. et al. Ultra-fast label-free quantification and comprehensive proteome coverage with narrow-window data-independent acquisition. *Nat. Biotechnol.* https://doi.org/10.1038/S41587-023-02099-7 (2024).

16. Wallmann, G. et al. AlphaDIA enables end-to-end transfer learning for feature-free proteomics. Preprint at *bioRxiv* https://doi.org/10.1101/2024.05.28.596182 (2024).

17. Min, J. et al. Phenyl-glutarimides: alternative cereblon binders for the design of PROTACs. *Angew. Chem. Int Ed. Engl.* **60**, 26663–26670 (2021).

18. Meier, F. et al. diaPASEF: parallel accumulation–serial fragmentation combined with data-independent acquisition. *Nat. Methods.* https://doi.org/10.1038/s41592-020-00998-0 (2020).

19. Soucy, T. A. et al. An inhibitor of NEDD8-activating enzyme as a new approach to treat cancer. *Nature* **458**, 732–736 (2009).

20. Sinitcyn, P. et al. Global detection of human variants and isoforms by deep proteome sequencing. *Nat. Biotechnol.* **41**, 1776–1786 (2023).

21. Donovan, K. A. et al. Thalidomide promotes degradation of SALL4, a transcription factor implicated in Duane Radial Ray syndrome. *eLife* **7**, e38430 (2018).

22. Verano, A. L. et al. Redirecting the neo-substrate specificity of cereblon-targeting PROTACs to helios. *ACS Chem. Biol.* **17**, 2404–2410 (2022).

23. Li, D. et al. Discovery of a dual WDR5 and Ikaros PROTAC degrader as an anti-cancer therapeutic. *Oncogene* **41**, 3328–3340 (2022).

24. Oleinikovas, V., Gainza, P., Ryckmans, T., Fasching, B. & Thomä, N. H. From thalidomide to rational molecular glue design for targeted protein degradation. *Annu. Rev. Pharmacol. Toxicol.* **64**, 291–312 (2024).

25. Jochem, M. et al. Degradome analysis to identify direct protein substrates of small-molecule degraders. *Cell Chem. Biol.* **32**, 192-200.e6 (2024).

26. Xu, G., Paige, J. S. & Jaffrey, S. R. Global analysis of lysine ubiquitination by ubiquitin remnant immunoaffinity profiling. *Nat. Biotechnol.* **28**, 868–873 (2010).

27. Steger, M. et al. Time-resolved in vivo ubiquitinome profiling by DIA-MS reveals USP7 targets on a proteome-wide scale. *Nat. Commun.* **12**, 1–13 (2021).

28. Crowe, C. et al. Mechanism of degrader-targeted protein ubiquitinability. *Sci. Adv.* **10**, eado6492 (2024).

29. Cloos, P. A. C. et al. The putative oncogene GASC1 demethylates tri- and dimethylated lysine 9 on histone H3. *Nature* **442**, 307–311 (2006).

30. Absmeier, E. et al. Specific recognition and ubiquitination of translating ribosomes by mammalian CCR4–NOT. *Nat. Struct. Mol. Biol.* **30**, 1314–1322 (2023).

31. He, X. et al. The zinc finger transcription factor Th-POK regulates CD4 versus CD8 T-cell lineage commitment. *Nature* **433**, 826–833 (2005).

32. Nickerson, M. L. et al. Mutations in a novel gene lead to kidney tumors, lung wall defects, and benign tumors of the hair follicle in patients with the Birt-Hogg-Dubé syndrome. *Cancer Cell* **2**, 157–164 (2002).

33. Fulcher, L. J. et al. The DUF1669 domain of FAM83 family proteins anchor casein kinase 1 isoforms. *Sci. Signal.* **11**, eaao2341 (2018).

34. Devault, A. et al. MAT1 ('menage à trois') a new RING finger protein subunit stabilizing cyclin H-cdk7 complexes in starfish and Xenopus CAK. *EMBO J.* **14**, 5027–5036 (1995).

35. Cheng, S.-W. G. et al. Interaction of cyclin-dependent kinase 12/CrkRS with cyclin K1 is required for the phosphorylation of the C-terminal domain of RNA polymerase II. *Mol. Cell. Biol.* **32**, 4691–4704 (2012).

36. Yamanaka, S. et al. A proximity biotinylation-based approach to identify protein-E3 ligase interactions induced by PROTACs and molecular glues. *Nat. Commun.* **13**, 1–17 (2022).

37. Baek, K. et al. Unveiling the hidden interactome of CRBN molecular glues with chemoproteomics. *Nat. Commun.* **16**, 6831 (2025).

38. Petzold, G., Fischer, E. S. & Thomä, N. H. Structural basis of lenalidomide-induced CK1α degradation by the CRL4CRBN ubiquitin ligase. *Nature* **532**, 127–130 (2016).

39. Krönke, J. et al. Lenalidomide induces ubiquitination and degradation of CK1α in del(5q) MDS. *Nature* **523**, 183–188 (2015).

40. Petzold, G. et al. Mining the CRBN Target Space Redefines Rules for Molecular Glue-induced Neosubstrate Recognition. *Science.* **389**, eadt6736 (2025).

41. Lv, L. et al. Discovery of a molecular glue promoting cdk12-ddb1 interaction to trigger cyclin k degradation. *eLife* **9**, 1–34 (2020).

42. Słabicki, M. et al. The CDK inhibitor CR8 acts as a molecular glue degrader that depletes cyclin K. *Nature* **585**, 293–297 (2020).

43. Mayor-Ruiz, C. et al. Rational discovery of molecular glue degraders via scalable chemical profiling. *Nat. Chem. Biol.* **16**, 1199–1207 (2020).

44. Matyskiela, M. E. et al. A novel cereblon modulator recruits GSPT1 to the CRL4CRBN ubiquitin ligase. *Nature* **535**, 252–257 (2016).

45. Alkalaeva, E. Z., Pisarev, A. V., Frolova, L. Y., Kisselev, L. L. & Pestova, T. V. In vitro reconstitution of eukaryotic translation reveals cooperativity between release factors eRF1 and eRF3. *Cell* **125**, 1125–1136 (2006).

46. Sperling, A. S. et al. Patterns of substrate affinity, competition, and degradation kinetics underlie biological activity of thalidomide analogs. *Blood* **134**, 160–170 (2019).

47. Huang, H.-T. et al. Ubiquitin-specific proximity labeling for the identification of E3 ligase substrates. *Nat. Chem. Biol.* **20**, 1227–1236 (2024).

48. Matyskiela, M. E. et al. SALL4 mediates teratogenicity as a thalidomide-dependent cereblon substrate. *Nat. Chem. Biol.* **14**, 981–987 (2018).

49. Meyer, C., Garzia, A., Morozov, P., Molina, H. & Tuschl, T. The G3BP1-family-USP10 deubiquitinase complex rescues ubiquitinated 40S subunits of ribosomes stalled in translation from lysosomal degradation. *Mol. Cell* **77**, 1193–1205.e5 (2020).

50. Teng, M. et al. Development of PDE6D and CK1α degraders through chemical derivatization of FPFT-2216. *J. Med. Chem.* **65**, 747–756 (2022).

51. Branon, T. C. et al. Efficient proximity labeling in living cells and organisms with TurboID. *Nat. Biotechnol.* **36**, 880–887 (2018).

52. Annunziato, S. et al. Molecular surface mimicry enables CRBN to target G3BP2 for degradation. Preprint at *bioRxiv* https://doi.org/10.1101/2025.04.30.651496 (2025).

53. Whetstine, J. R. et al. Reversal of histone lysine trimethylation by the JMJD2 family of histone demethylases. *Cell* **125**, 467–481 (2006).

54. Trojer, P. et al. Dynamic histone H1 isotype 4 methylation and demethylation by histone lysine methyltransferase G9a/KMT1C and the Jumonji domain-containing JMJD2/KDM4 proteins. *J. Biol. Chem.* **284**, 8395–8405 (2009).

55. Lee, D. H. et al. Advances in histone demethylase KDM4 as cancer therapeutic targets. *FASEB J.* **34**, 3461–3484 (2020).

56. Wu, Q. et al. Recent advances with KDM4 inhibitors and potential applications. *J. Med Chem.* **65**, 9564–9579 (2022).

57. Walters, Z. S. et al. Role for the histone demethylase kdm4b in rhabdomyosarcoma via cdk6 and ccna2: Compensation by kdm4a and apoptotic response of targeting both kdm4b and kdm4a. *Cancers* **13**, 1734 (2021).

58. Ziegler, W. H., Liddington, R. C. & Critchley, D. R. The structure and regulation of vinculin. *Trends Cell Biol.* **16**, 453–460 (2006).

59. Wang, E. S. et al. Acute pharmacological degradation of Helios destabilizes regulatory T cells. *Nat. Chem. Biol.* **17**, 711–717 (2021).

60. Gupta, N. et al. Stress granule-associated protein G3BP2 regulates breast tumor initiation. *Proc. Natl. Acad. Sci. USA* **114**, 1033–1038 (2017).

61. Takayama, K. I., Suzuki, T., Fujimura, T., Takahashi, S. & Inoue, S. Association of USP10 with G3BP2 inhibits p53 signaling and contributes to poor outcome in prostate cancer. *Mol. Cancer Res.* **16**, 846–856 (2018).

62. Rappsilber, J., Ishihama, Y. & Mann, M. Stop and go extraction tips for matrix-assisted laser desorption/ionization, nanoelectrospray, and LC/MS sample pretreatment in proteomics. *Anal. Chem.* https://doi.org/10.1021/ac026117i (2003).

63. Szyrwiel, L., Sinn, L., Ralser, M. & Demichev, V. Slice-PASEF: fragmenting all ions for maximum sensitivity in proteomics. Preprint at *bioRxiv* https://doi.org/10.1101/2022.10.31.514544 (2022).

64. Skowronek, P., Wallmann, G., Wahle, M., Willems, S. & Mann, M. An accessible workflow for high-sensitivity proteomics using parallel accumulation–serial fragmentation (PASEF). *Nat. Protoc.* https://doi.org/10.1038/s41596-024-01104-w (2025).

65. Singh, S. et al. Targeting KDM4 for treating PAX3-FOXO1–driven alveolar rhabdomyosarcoma. *Sci. Transl. Med.* **14**, eabq2096 (2022).

66. Lier, S. et al. A novel Cereblon E3 ligase modulator with antitumor activity in gastrointestinal cancer. *Bioorg. Chem.* **119**, 105505 (2022).

67. Brown, L. Y., Dong, W. & Kantor, B. An improved protocol for the production of lentiviral vectors. *STAR Protoc.* **1**, 100152 (2020).

68. Cox, J. et al. Accurate proteome-wide label-free quantification by delayed normalization and maximal peptide ratio extraction, termed MaxLFQ. *Mol. Cell Proteom.* **13**, 2513 (2014).

69. Ritchie, M. E. et al. Limma powers differential expression analyses for RNA-sequencing and microarray studies. *Nucleic Acids Res.* https://doi.org/10.1093/nar/gkv007 (2015).

70. Varadi, M. et al. AlphaFold Protein Structure Database in 2024: providing structure coverage for over 214 million protein sequences. *Nucleic Acids Res.* **52**, D368–D375 (2024).

71. Jumper, J. et al. Highly accurate protein structure prediction with AlphaFold. *Nature* **596**, 583–589 (2021).

Acknowledgements

Author contributions

M.S. designed and performed the experiments, analyzed and interpreted the data, prepared the figures, and wrote the manuscript. B.Sch. developed the data analysis pipeline and interpreted the data. B.Sh. analyzed and interpreted the data, edited the manuscript, and prepared the figures. U.O. analyzed and interpreted the data. H.D. and Z.R. conceived the study, designed the experiments, analyzed and interpreted the data, and wrote the manuscript. A.H.B., S.M., T.G., and D.B. performed the experiments and co-developed the ubiquitinomics and TurboID assays. V.D. provided software tools essential for raw data processing. G.N. designed the molecular glue library, selected compounds for proteomics-directed medicinal chemistry, and edited the manuscript. K.M. designed and synthesized compounds. Z.S., J.P., and L.Y. synthesized and purified compounds. A.A. obtained protein constructs, and M.A. developed ternary complex assays. A.M. performed assay profiling of compounds. Q.W. performed the experiments, analyzed and interpreted the data, edited the manuscript, and prepared the figures. Y.J. designed and supervised the study, interpreted the data, and was involved in manuscript writing and editing. All authors read and approved the final manuscript.

Competing interests

Additional information

Supplementary information The online version contains supplementary material available at https://doi.org/10.1038/s41467-025-62829-0.

Correspondence and requests for materials should be addressed to Jun Yang, Henrik Daub or Zoran Rankovic.

Peer review information *Nature Communications* thanks Danette Daniels, Tatsuya Sawasaki, and the other anonymous reviewer(s) for their contribution to the peer review of this work. A peer review file is available.

Reprints and permissions information is available at http://www.nature.com/reprints

Publisher's note Springer Nature remains neutral with regard to jurisdictional claims in published maps and institutional affiliations.